



Stability based approach to design cold-water pipe (CWP) for ocean thermal energy conversion (OTEC)

Ristiyanto Adiputra*, Tomoaki Utsunomiya

Department of Marine Systems Engineering, Kyushu University, Fukuoka 819-0395, Japan

ARTICLE INFO

Keywords:

Ocean Thermal Energy Conversion (OTEC)
Cold water pipe (CWP)
Critical velocity assessment
Fluid-structure interaction

ABSTRACT

Cold-water pipe (CWP) is a novel, most-challenging component of Ocean Thermal Energy Conversion (OTEC) floating structure which is installed to transport the deep seawater to the board. For commercial scale, the transported seawater flow rate will be in the order of $10^2 \text{ m}^3/\text{s}$. This large amount of internal flow may trigger instability which leads to the failure of CWP. Considering this issue, the present paper aims to design commercial-scale OTEC CWP focusing on the effects of internal flow to the stability of the pipe. The design analysis is deliberated to select the pipe material, top joint configuration (fixed, flexible, pinned) and bottom supporting system (with and without clump weight). Initially, the analytical solution is built by taking into account the components of the pipe dynamics. Separately, a fully coupled fluid-structure interaction analysis between the pipe and the ambient fluid is carried out using ANSYS interface. Using scale models, the results obtained from the analytical solution are compared with the ones from numerical analysis to examine the feasibility of the analytical solution. After being verified, the analytical solution is used to observe the dynamic behavior of the CWP for 100 MW-net OTEC power plant in the full-scale model. The results yield conclusions that pinned connection at the top joint is preferable to decrease the applied stress, clump weight installation is necessary to reduce the motion displacement and Fiber Reinforced Plastic (FRP) is the most suitable material among the examined materials.

1. Introduction

Ocean Thermal Energy Conversion is a process of harvesting energy from the ocean by utilizing the temperature difference between surface warm water and deep cold water [1,2]. The heat from surface warm water is used to transform the working fluid from a liquid into gas form. To maintain the cycle, the cold water is required to retransform the working fluid back to the liquid form after being used to drive the turbine generator [1]. From the OTEC feasibility study, the temperature difference between surface warm water and deep cold water must be at least 20°C in order to reach the minimum required efficiency [2].

Preliminary studies on the design of a 100 MW-net OTEC power plant which previously carried out by the authors resulted a baseline design of the floating structure from oil tanker ship conversion as shown in Fig. 1 [3]. In general, the main novelty of the OTEC floating structure compared with the other utilization is the installation of a suspended pipe transporting deep cold seawater (Cold Water Pipe; CWP) onto the floating structure [4–7]. To produce 100 MW-net electricity, the CWP must be lengthened to reach 800 m depth with an inner diameter of 12 m [3]. As the water comes from the bottom part of the

pipe, the pipe must be installed in a free hanging configuration. This condition causes the top joint connection the only supporting point to support the integrity of the pipe from the applied stress. Another challenge is the effect of the self-excitation due to internal flow to the stability of the riser. Additionally, the cost estimation study for OTEC development states that the cost to build the CWP is approximately 15–20% of the total capital cost [8].

The important role of OTEC CWP to the success of OTEC installation and operation is undeniable by the fact that numerous OTEC projects failed and then abandoned due to CWP problems such as Rio de Janeiro OTEC project in 1935 and even India OTEC project in 2003 [1,5]. Until now, the immature design and unsettled technology of the CWP are the main reasons why OTEC development still gets stuck in the pilot project [5].

As typical marine riser, the issues of the CWP design can be divided into three main problems [9]. The first issue is the strength analysis including extreme and collapse analysis. Based on this view, several works on OTEC riser have been carried out by Nihous and Vega [4] and Lockheed Martin [5,6]. An attempt to propose the concept of CWP for 100 MW-net OTEC power plant was done by Nihous and Vega in 1993

* Corresponding author.

E-mail address: adiputra@nams.kyushu-u.ac.jp (R. Adiputra).

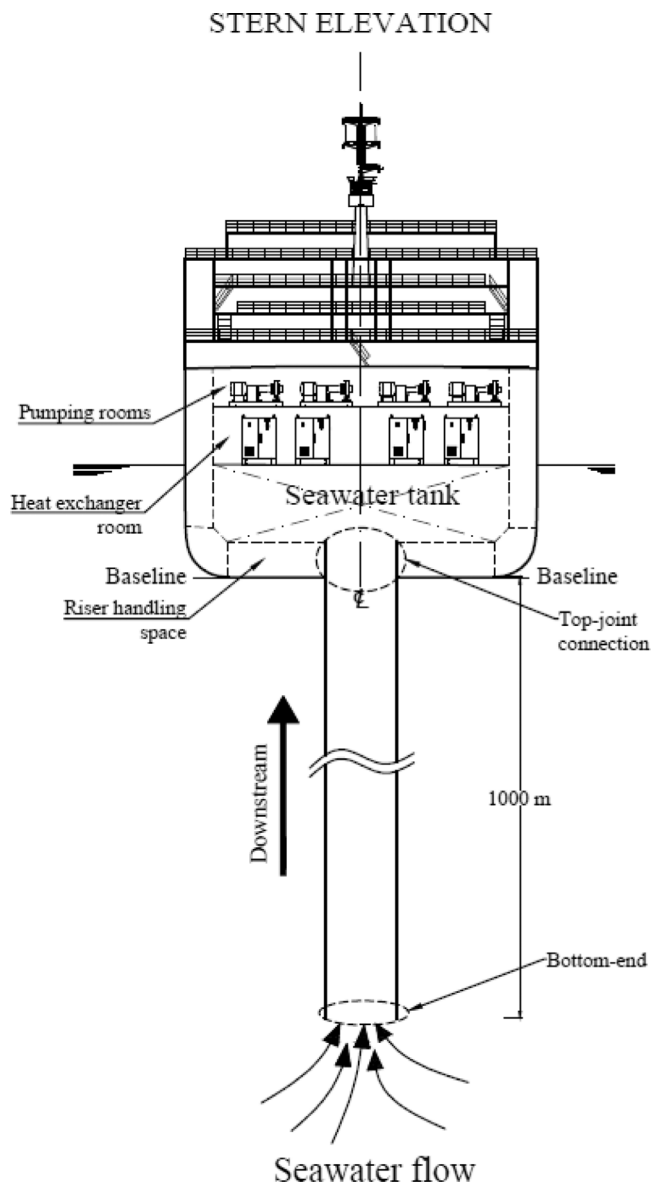


Fig. 1. Sketch of the plattform.

[4]. They conceptualized the CWP with a diameter of 10 m from fiber reinforced plastic considering the axial strain and the top joint stress. Far after Nihous and Vega, Lockheed Martin gave additional consideration to design the CWP by including the additional applied loads caused by external pressure, platform rotation, etc. [5,6]. The second issue is the vessel-CWP coupled analysis problem. Most recent work on this issue was done by He et al. in 2018 [10]. He developed robust adaptive boundary controllers to analyze the coupled vibration problem between the vessel, CWP and the ballast linked. Albeit the main intention is not for OTEC riser, taking into account the coupled effects between the submerged riser and the surface vessel, He et al. [11] also introduced the concept of top tension control to increase the durability of the top joint connection which is also a crucial issue for OTEC riser. The third problem is regarding the vibration of the pipe (vortex induced vibration and internal-flow induced vibration) which then leads to the fatigue analysis problem. This problem has not been considered in the previous mentioned works. However, researches on the pipe aspirating fluid have analytically, numerically and experimentally proven that the internal flow could also trigger instability of the pipe [12–17].

By the fact that CWP is required to transport a large amount of seawater, it is crucial to include the effect of the internal flow to the

design consideration [18]. In [18], Zhang et al. vastly discussed the mechanical problems in OTEC as internal and external mechanical problems. The internal mechanical problem regards to the steam turbine issues and the external mechanical problem refers to the hydrodynamic issues on the CWP. In the external mechanical problem analysis, the CWP is modeled as a simple beam with top end and lumped mass at the bottom. In collaboration with the winds, waves, and currents, the internal velocity effect to the riser vibration is examined in term of the lateral displacement. Nevertheless, the internal effect modeling in the built general motion equation in [18] seems insufficient considering the fluid phenomena on the typical submerged riser conveying fluid [12–17]. Thus, a more detailed model is necessary to exhaustively examine the effect of the internal flow to the OTEC riser stability. With respect to this matters, this paper will solely focus on the internal velocity effect and its ramification to the preliminary design of the OTEC riser.

Literally, the CWP can be described as a submerged free hanging pipe conveying seawater subjected to the top stress and axial strain. The study on critical velocity assessment of free hanging riser conveying fluid has been done by many researchers in these last decades. The works mainly refer, extend and develop the comprehensive theory by Païdoussis and Issid [12] for various pipe configurations, boundary conditions and applied loads. As the aim of this study is to design a pipe conveying seawater for OTEC utilization, the review will be highlighted and focused on the works which have significant correlation to portray the dynamic behavior of OTEC CWP. More detail record progress of the works on pipe conveying fluid can be found from the introduction of corresponded published papers such as in [13–15].

The numerical simulation of free hanging riser conveying fluid was carried out by Giacobbi et al. in 2008 [13]. In 2010, Giacobbi enhanced the methodology to more clearly duplicate the real condition of pipe conveying fluid characteristic [14]. Then, in 2012, Giacobbi et al. reused the simulation process in [14] to analyze a riser discharging and aspirating fluid and compare the results with experimental and analytical results [15]. In [13–15], the effect of added mass and drag coefficient which are dominant in the submerged pipe conveying fluid was disregarded. Although the used analytical solution cannot cover the dynamic components of OTEC CWP, it gives an overview how to undergo the numerical simulation and how to compare the results of numerical and analytical solutions using bifurcation curves.

In 2005, Kuiper and Metrikine specifically investigated the effect of the drag coefficient and its contribution to the stability of a submerged pipe conveying fluid [16]. Even though the initial intention is to question Païdoussis and Issid's statement which valuing the effect of inlet depressurization as the reason why flutter does not take place in small velocity, the built equation also adroitly captures how to model the effect of the ambient fluid to the dynamic motion in convenient way.

In the case of boundary condition modeling, to observe its effects to the dynamic behavior of a simple fluid-conveying pipe model, Liang et al. proposed a methodology which is able to incorporate the differential quadrature method and inverse Laplace transform [17]. The analysis was done by varying the boundary conditions at the end edges of the pipe and resulting a conclusion that the dynamic behavior firmly depends on the boundary conditions at the both ends.

In this paper, the process of the numerical simulation from the former researches [13–15] is adapted and then modified to vary the boundary conditions at the top- and bottom ends of the pipe. Then the general analytical model proposed by Kuiper and Metrikine [16] is modified by taking into account the hysteretic damping to the dynamic motion components. The added mass and adapted drag coefficient which is assumed in [16] will be determined using numerical analysis for the conditions with and without clump weight. To obtain the general solution, the boundary conditions are varied by adapting the boundary condition modeling as used in [16,17]. In order to verify the analytical solution, the comparison method used in [15] will be

employed. Finally, the verified analytical solution will be used to design the CWP in full-scale models. As additional results, the vibration frequency is also investigated here. Even though in this study the vibration frequency will not be directly used to determine the acceptance of the particular cases, it will be used to predict the fatigue life of the CWP for the future work.

In brief, this paper proposes an analytical solution to include the significant effect of the internal flow to the dynamic motions of the CWP which has not been genuinely considered in the existing published studies on OTEC riser. To emphasize the basic understanding and sharpen the analysis in a deep and vast manner, even though the riser is also subject to external flow, the concern of this paper will be limited on the internal flow effect on the stability of riser in the term of the critical seawater transport velocity and the applied stress. As efforts to increase the integrity and ensure the survivability of the CWP, this paper also examines the feasible supporting system at the top joint connection and at the bottom end of the pipe.

The first aim of this study is to propose an analytical solution and then verify it using numerical simulation and experimental result from the previous publication. After the confidant of the analytical solution has been proven, the analytical solution is used to examine the OTEC CWP for 100 MW-net capacity. As final result, this paper yields a preliminary design of the 100 MW-net OTEC CWP including the material choice, type of the top-end supporting system and the required weight of the clump at the bottom end of the riser.

Besides its main purpose of introducing the effect of the internal flow for the OTEC riser design, through this paper, the theory on the free hanging riser conveying fluid which has been studied in the last decades will be brought from the pure theory to the design practice. As new founded applications of offshore riser conveying fluid have been recognized, the interest of its fundamental knowledge and application would be drawn more intentionally.

2. Case configurations and methods

Based on the sketch of CWP as shown in Fig. 1, the CWP can be modeled as a top-tensioned, submerged, seawater-aspirating pipe subjected to the axial stress due to self-weight and bending stress due to dynamic motion. To be delivered from the subsurface to the floating structure, the seawater comes through an inlet point at the bottom end of the pipe. As the bottom-end cannot be attached to the seabed, there is no supporting system at the bottom-end to reinforce the riser. The term 'top-tensioned' is associated with this free bottom-end condition which makes the stress concentrated at the top-end joint connection between the pipe and the floating structure.

The term 'submerged' brings an implication that during its dynamic motion, the surrounding fluid, in this case also seawater, will give reaction opposite to the direction of the motion. This reaction is well-known as hydrodynamic added mass and drag force. During the motion, as the pipe displaces, the bending stress will occur. The stress is sum up of the axial stress due to self-weight and the bending stress due to the dynamic motion.

The riser length, the riser inner diameter, and the minimum required flow rate velocity to determine the acceptance of the case configuration are calculated based on the results of the on-site experiment at Mentawai island, Indonesia [3]. But for the thickness, its value is estimated based on the required flexural rigidity of CWP which assessed by Nihous and Vega [4]. The main scantlings and material properties of the full-scale CWP are determined as shown in Table 1.

Considering the pipe materials, the models are respectively named as pipe A, pipe B, and pipe C. Due to limited computational capability, it is impossible to carry out the numerical simulation using full-scale models. Thus, the numerical simulation models are defined by scaling down the real CWP size with a factor of 0.1, 0.2, 0.3 and 0.4. The model scantlings are varied incrementally to investigate how the dynamic behavior changes due to the change of the pipe sizes and then the

Table 1
Material properties and main scantlings of CWP in full scale.

Properties		Pipe A	Pipe B	Pipe C
Material		Steel	Aluminum	FRP
Inner diameter	(m)	12	12	12
Thickness	(cm)	6	10	16
Section area	(m ²)	2.27	3.78	6.03
Length	(m)	1000	1000	1000
Young's modulus	(MPa)	205,000	72,000	13,776
Yield stress	(MPa)	350	240	550
Dry weight	(N/m)	173,247	100,116	71,854
Wet weight	(N/m)	150,481	62,109	9407
Total weight	(N)	150.5×10^6	62×10^6	9.41×10^6
Hysteretic damping loss factor		1.5×10^{-3}	1×10^{-4}	1.6×10^{-2}

[19–22]

results are used to predict the hydrodynamic coefficients of the full-scale models. For convenience, here onward, the simulation models are named with two initial characters as 'XY'. 'X' is an alphabet referring to the type of the material and 'Y' is a number pointing the scale factor as 0.Y. For instance, pipe A3 means a pipe with material properties of pipe A and the scantlings which are calculated by scaling down the real size of the CWP with scale factor 0.3, that is, pipe with the length of 300 m, the inner diameter of 3.6 m and the thickness of 1.8 cm.

The supporting system at the top joint connection is investigated thoroughly by examining possible solutions including fixed joint, pinned joint and flexural joint with varied stiffness values. At the bottom configuration, the cases will be built with and without considering clump weight installation. The sketches of the case configuration due to variation of the supporting systems are listed in Fig. 2 and will be explained in detail in Section 4.2.

First, the numerical simulation is carried out for models with scale factor 0.1, 0.2 and 0.3. The results are added mass coefficient, adapted drag coefficient, and the motion amplitude. Considering the results, the sensitivity of motion amplitude on the variables can be assessed. Using the value of added mass and adapted drag coefficient of models with scale factor 0.1, 0.2 and 0.3, the added mass and adapted drag coefficient of models with scale factor 0.4 can be forecasted. Inputting these values to the analytical simulation, the critical velocity of models with scale factor 0.4 can be determined. Separately, the numerical simulation analysis is also done for models with scale factor 0.4. Comparing the results from analytical and numerical simulation, the acceptance of the analytical model can be concluded. After being verified, the analytical solution is used for full-scale models.

The term analytical solution here refers to a specific definition or can be broadly described as 'semi-analytical' as in the process, MATLAB is used as a helping tool. In the case of the numerical simulation, Ansys interface software is employed to undergo the fluid-structure simulation.

3. Analytical simulation

3.1. Governing general equation

In the analytical analysis, the motion is observed around the straight configuration and under the following assumptions: (1) the motion of the riser is in a two-dimensional plane; (2) length over the diameter of the riser is large enough so that the system can be investigated based on Euler–Bernoulli theory. The principal bases of the Euler–Bernoulli beam system modeling for submerged marine structure can be found in [23]; (3) The plug-flow assumption is used to model the internal fluid movement; (4) the material damping is considered based on the hysteretic damping model; (5) the motion of the floating structure is not taken into account; (6) the main flow of the velocity along the riser is constant; (7) the external forces and friction force between riser and fluid are neglected.

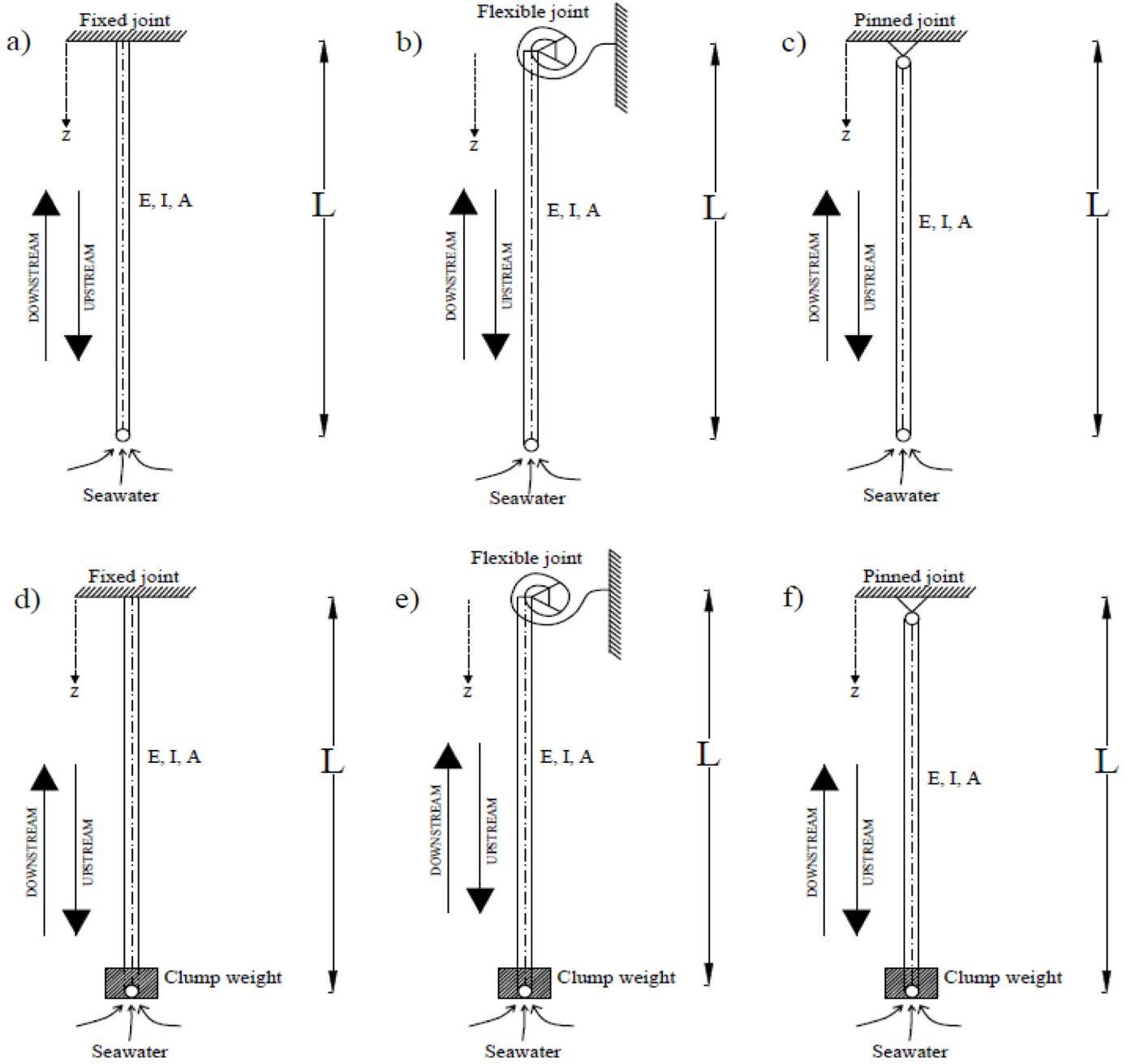


Fig. 2. Sketch of the supporting systems. (a) fixed-free; (b) flexible-free; (c) pinned-free; (d) fixed-free with clump weight; (e) flexible-free with clump weight; (f) pinned-free with clump weight.

The riser is tubular with an outer diameter D_o , inner diameter D_i , the length L , density ρ_r , and cross-sectional area A_r . The riser is submerged in the fluid with a density ρ_f and subject to gravitational acceleration g . At time t and at the distance from the top joint z , the transverse displacement of the cross section is denoted as $w(z, t)$. The equation of its undamped lateral motion in the frame of a linearized model can be obtained as [16].

$$EI \frac{\partial^4 w}{\partial z^4} - 2u_f m_f \frac{\partial^2 w}{\partial t \partial z} + (m_f + m_r + m_a) \frac{\partial^2 w}{\partial t^2} + \left(-T_{BT} \left(1 - \frac{z}{L} \right) - W_c + m_f u_f^2 \right) \frac{\partial^2 w}{\partial z^2} + \frac{T_{top}}{L} \frac{\partial w}{\partial z} + \frac{1}{2} \rho_f D_o \tilde{C}_d \frac{\partial w}{\partial t} = 0 \quad (1)$$

where EI is the flexural rigidity of the pipe, u_f the velocity of seawater transport, m_f , m_r , and m_a mass per unit length of the fluid, bare-riser and

added mass, respectively, \tilde{C}_d adapted drag coefficient, T_{BT} wet weight of bare riser (without clump weight) calculated as $(\rho_r - \rho_f)A_r g L$, and T_{top} the total top tension (with clump weight) determined as $T_{BT} + W_c$. If installed, W_c is the weight of the clump at the bottom. In this equation, the weight of the bare riser is distributed equally along the riser but the weight of the clump is treated as a point mass located at the bottom end of the pipe.

If the hysteretic damping of the material with loss factor μ at motion frequency Ω is considered, the Eq. (1) reads

$$EI \left[1 + \left(\frac{\mu}{\Omega} \right) \frac{\partial}{\partial t} \right] \frac{\partial^4 w}{\partial z^4} - 2u_f m_f \frac{\partial^2 w}{\partial t \partial z} + (m_f + m_r + m_a) \frac{\partial^2 w}{\partial t^2} + \left[-T_{BT} \left(1 - \frac{z}{L} \right) - W_c + m_f u_f^2 \right] \frac{\partial^2 w}{\partial z^2} + \frac{T_{top}}{L} \frac{\partial w}{\partial z} + \frac{1}{2} \rho_f D_o \tilde{C}_d \frac{\partial w}{\partial t} = 0 \quad (2)$$

To solve Eq. (2) in a convenient way, it had better rewrite Eq. (2) into dimensionless form by introducing the dimensionless variables as

$$\begin{aligned} \Delta &= w/L; \quad \Gamma = z/L; \quad \tau = t\sqrt{EI/m_f + m_r + m_a}/L^2; \\ \omega &= \Omega L^2 \sqrt{m_f + m_r + m_a}/EI \\ v &= u_f \sqrt{m_f/T_{top}}; \quad \theta_{top} = T_{top}L^2/EI; \quad \theta_{BT} = T_{BT}L^2/EI; \\ \theta_C &= W_c L^2/EI; \\ \zeta &= L\sqrt{m_f T_{top}}/\sqrt{EI(m_f + m_r + m_a)}; \\ \xi &= \rho_f D_o \tilde{C}_d L^2/(2\sqrt{EI(m_f + m_r + m_a)}); \\ \Lambda &= \alpha\sqrt{EI/m_f + m_r + m_a}/L^2 \end{aligned}$$

Inserting all of the dimensionless variables above to Eq. (2), the new statement of the problem can be rewritten as

$$\begin{aligned} \left[1 + \left(\frac{\mu}{\omega} \right) \frac{\partial}{\partial \tau} \right] \frac{\partial^4 \Delta}{\partial \Gamma^4} + \theta_{top} v^2 \frac{\partial^2 \Delta}{\partial \Gamma^2} - (\theta_C + \theta_{BT}) \frac{\partial^2 \Delta}{\partial \Gamma^2} + \theta_{BT} \Gamma \frac{\partial^2 \Delta}{\partial \Gamma^2} + \theta_{top} \frac{\partial \Delta}{\partial \Gamma} \\ - 2\zeta v \frac{\partial^2 \Delta}{\partial \Gamma \partial \tau} + \xi \frac{\partial \Delta}{\partial \tau} + \frac{\partial^2 \Delta}{\partial \tau^2} = 0 \end{aligned} \quad (3)$$

Eq. (3) still has variable Γ and variable τ . The next step is simplifying Eq. (3) by assuming that

$$\Delta(\Gamma, \tau) = \Pi(\Gamma)e^{\lambda\tau} \quad (4)$$

then, Eq. (3) reads

$$\begin{aligned} (1 - i\mu) \frac{\partial^4 \Pi}{\partial \Gamma^4} + (\theta_{top} v^2 - \theta_C - \theta_{BT}) \frac{\partial^2 \Pi}{\partial \Gamma^2} + \theta_{BT} \Gamma \frac{\partial^2 \Pi}{\partial \Gamma^2} + (\theta_{top} - 2\lambda\zeta v) \frac{\partial \Pi}{\partial \Gamma} \\ + (\lambda\xi + \lambda^2) \Pi = 0 \end{aligned} \quad (5)$$

From Eq. (4), it can be simply understood that the system becomes unstable if the eigenvalues λ has a positive real part. At the unstable state, the stability happens due to flutter when $\text{im}(\lambda) \neq 0$ and by static divergence if $\text{im}(\lambda) = 0$. Additionally, from Eq. (5), it can be shown that the third term of the dimensionless differential equation has a coefficient that depends on Γ . This brings an implication that the solution of eigenvalues cannot be solved by sinusoidal equation. Huang and Dareing [24] suggested that this kind of a differential form can be solved by a solution in the form of power series expansion as

$$\Pi(\Gamma) = \sum_{n=0}^{\infty} a_n \Gamma^n \quad (6)$$

where the constants a_n are some coefficients. If almost all of the a_n is equal to zero, the equation can be a so-called polynomial function, but if many of a_n are nonzero, the convergence of the power series must be considered.

The next part will be focused on how to obtain the value of coefficients a_n . By substituting Eq. (6) to Eq. (5), a new equation can be derived. This new produced equation consists of several terms based on its variables ($\Gamma^n, \Gamma^{n-1}, \Gamma^{n-2}, \dots, \Gamma^0$). As the right-hand side of Eq. (5) is zero, the product summation of all terms will be equal to zero. To make the sum of all terms zero, each term in the series must be also equal to zero. Considering this condition, a recurrence relation of coefficients a_n can be derived as

$$\begin{aligned} a_n = \left(\frac{i\mu}{n} \right) a_{n-1} + \left(\frac{-\theta_{top} v^2 + \theta_C + \theta_{BT}}{n(n-1)} \right) a_{n-2} \\ + \left(\frac{-\theta_{BT}(n-2) - \theta_{top} + 2\zeta v \lambda}{n(n-1)(n-2)} \right) a_{n-3} \\ + \left(\frac{-\lambda\xi + \lambda^2}{n(n-1)(n-2)(n-3)} \right) a_{n-4}, \quad (n \geq 4) \end{aligned} \quad (7)$$

Using Eq. (7), the coefficients a_n can be calculated for n starting from 4 to infinity. In the aim to change the starting n from four to zero, the recurrence relation of Eq. (7) is modified so then a_n can be expressed as a linear summation of a_0, a_1, a_2, a_3 as

$$a_n = W_n a_0 + X_n a_1 + Y_n a_2 + Z_n a_3, \quad (n \geq 0) \quad (8)$$

where W_n, X_n, Y_n, Z_n can be calculated as

$$\begin{aligned} \begin{bmatrix} W_n \\ X_n \\ Y_n \\ Z_n \end{bmatrix} = \frac{i\mu}{n} \begin{bmatrix} W_{n-1} \\ X_{n-1} \\ Y_{n-1} \\ Z_{n-1} \end{bmatrix} + \frac{-\theta_{top} v^2 + \theta_C + \theta_{BT}}{n(n-1)} \begin{bmatrix} W_{n-2} \\ X_{n-2} \\ Y_{n-2} \\ Z_{n-2} \end{bmatrix} \\ + \frac{-\theta_{BT}(n-2) - \theta_{top} + 2\zeta v \lambda}{n(n-1)(n-2)} \begin{bmatrix} W_{n-3} \\ X_{n-3} \\ Y_{n-3} \\ Z_{n-3} \end{bmatrix} \\ + \frac{-(\lambda\xi + \lambda^2)}{n(n-1)(n-2)(n-3)} \begin{bmatrix} W_{n-4} \\ X_{n-4} \\ Y_{n-4} \\ Z_{n-4} \end{bmatrix} \end{aligned} \quad (9)$$

The initial condition of Eq. (9) can be defined based on the transformation of Eq. (7) to Eq. (8) as

$$\begin{bmatrix} W_0 & W_1 & W_2 & W_3 \\ X_0 & X_1 & X_2 & X_3 \\ Y_0 & Y_1 & Y_2 & Y_3 \\ Z_0 & Z_1 & Z_2 & Z_3 \end{bmatrix} = \begin{bmatrix} 1 & 0 & 0 & 0 \\ 0 & 1 & 0 & 0 \\ 0 & 0 & 1 & 0 \\ 0 & 0 & 0 & 1 \end{bmatrix} \quad (10)$$

Finally, by replacing a_n in Eq. (6) with Eq. (9), the form of Eq. (6) will be

$$\Pi(\Gamma) = \sum_{n=0}^{\infty} (W_n a_0 + X_n a_1 + Y_n a_2 + Z_n a_3) \Gamma^n \quad (11)$$

3.2. Boundary condition and general solutions

To find the four unknown $a_j, j = 0, .3$, Eq. (11) must be substituted into boundary condition which differs depending on the case of the end-tip connection. As mentioned briefly in Section 2, six combinations of pipe end boundary conditions are investigated including: fixed-free (Fig. 2a), flexible-free (Fig. 2b), pinned-free (Fig. 2c), fixed-clump weight (Fig. 2d), flexible-clump weight (Fig. 2e), pinned-clump weight (Fig. 2f). The boundary conditions can be expressed as follows:

Boundary conditions at the top end of the pipe

$$\text{Fixed joint: } w(0, t) = 0; EI \frac{\partial w}{\partial z} \Big|_{z=0} = 0 \quad (12)$$

$$\text{Flexible joint: } w(0, t) = 0; EI \frac{\partial^2 w}{\partial z^2} \Big|_{z=0} = C_{\beta} \frac{\partial w}{\partial z} \Big|_{z=0} \quad (13)$$

$$\text{Pinned joint: } w(0, t) = 0; EI \frac{\partial^2 w}{\partial z^2} \Big|_{z=0} = 0 \quad (14)$$

Boundary conditions at the bottom end of the pipe

$$\text{Free: } EI \frac{\partial^2 w}{\partial z^2} \Big|_{z=L} = 0; EI \frac{\partial^3 w}{\partial z^3} \Big|_{z=L} = 0 \quad (15)$$

$$\text{Clump weight: } EI \frac{\partial^2 w}{\partial z^2} \Big|_{z=L} = 0; EI \frac{\partial^3 w}{\partial z^3} \Big|_{z=L} = \frac{W_c}{L} w(L, t) \quad (16)$$

where C_{β} is the stiffness of the rotational spring and W_c is the weight of the bottom clump. Transforming the boundary condition into dimensionless form, the new statement of the boundary condition can be explained as:

Dimensionless expression of the boundary conditions at the top end of the pipe

$$\text{Fixed joint: } \Delta(0, \tau) = 0; \frac{\partial \Delta}{\partial \Gamma} \Big|_{\Gamma=0} = 0 \quad (17)$$

$$\text{Flexible joint: } \Delta(0, \tau) = 0; \left. \frac{\partial^2 \Delta}{\partial \Gamma^2} \right|_{\Gamma=0} = K \left. \frac{\partial \Delta}{\partial \Gamma} \right|_{\Gamma=0} \quad (18)$$

$$\text{Pinned joint: } \Delta(0, \tau) = 0; \left. \frac{\partial^2 \Delta}{\partial \Gamma^2} \right|_{\Gamma=0} = 0 \quad (19)$$

Dimensionless expression of the boundary conditions at the bottom end of the pipe

$$\text{Free: } \left. \frac{\partial^2 \Delta}{\partial \Gamma^2} \right|_{\Gamma=1} = 0; \left. \frac{\partial^3 \Delta}{\partial \Gamma^3} \right|_{\Gamma=1} = 0 \quad (20)$$

$$\text{Clump weight: } \left. \frac{\partial^2 \Delta}{\partial \Gamma^2} \right|_{\Gamma=1} = 0; \left. \frac{\partial^3 \Delta}{\partial \Gamma^3} \right|_{\Gamma=1} = K_C \Delta(L, \tau) \quad (21)$$

K is defined as $C_R L / EI$ and K_C is defined as $W_c L^2 / EI$. The next step is inserting the boundary condition into Eq. (11). This yields four linear algebraic equation with respect to a_j , $j = 0, .3$.

The method to derive the general solution using these boundary expressions is basically similar for all cases. For example, let's call the case 2 where the riser is a free hanging riser subjected to a rotational restraint at the end-tip of the downstream point. In this case, Eqs. (18) and (20) are used. For the first and the second boundary condition (Eq. (18)), it can be concluded that

$$a_0 = 0 \text{ and } a_2 = \frac{K}{2} a_1 \quad (22)$$

Then, Eq. (22) along with the third and the fourth boundary conditions (Eq. (20)) are substituted into Eq. (11), so the new relationship will yield as

$$a_1 \left(\sum_{n=2}^{\infty} X_n n(n-1) + a_2 \sum_{n=2}^{\infty} Y_n n(n-1) \right) + a_3 \sum_{n=2}^{\infty} Z_n n(n-1) = 0 \quad (23)$$

$$a_1 \left(\sum_{n=3}^{\infty} X_n n(n-1)(n-2) + a_2 \sum_{n=3}^{\infty} Y_n n(n-1)(n-2) \right) + a_3 \sum_{n=3}^{\infty} Z_n n(n-1)(n-2) = 0 \quad (24)$$

Eqs. (23) and (24) have a non-trivial solution if the determinant of the following matrix is equal to zero.

$$\begin{vmatrix} \frac{K}{2} & -1 & 0 \\ \sum_{n=2}^{\infty} X_n n(n-1) & \sum_{n=2}^{\infty} Y_n n(n-1) & \sum_{n=2}^{\infty} Z_n n(n-1) \\ \sum_{n=3}^{\infty} X_n n(n-1)(n-2) & \sum_{n=3}^{\infty} Y_n n(n-1)(n-2) & \sum_{n=3}^{\infty} Z_n n(n-1)(n-2) \end{vmatrix} = 0 \quad (25)$$

Using Eq. (25), the eigenvalues of Eq. (4) can be obtained for case 2. By repeating the method for cases 2, the general solutions of the other cases can be expressed as

$$\text{Fixed-free (case 1)} \quad \begin{vmatrix} (\sum_{n=2}^{\infty} Y_n n(n-1)) & (\sum_{n=2}^{\infty} Z_n n(n-1)) \\ (\sum_{n=3}^{\infty} Y_n n(n-1)(n-2)) & (\sum_{n=3}^{\infty} Z_n n(n-1)(n-2)) \end{vmatrix} = 0 \quad (26)$$

$$\text{Pinned-free (case 3)} \quad \begin{vmatrix} (\sum_{n=2}^{\infty} X_n n(n-1)) & (\sum_{n=2}^{\infty} Z_n n(n-1)) \\ (\sum_{n=3}^{\infty} X_n n(n-1)(n-2)) & (\sum_{n=3}^{\infty} Z_n n(n-1)(n-2)) \end{vmatrix} = 0 \quad (27)$$

Fixed-clump weight (case 4)

$$\begin{vmatrix} (\sum_{n=2}^{\infty} n(n-1)) & (\sum_{n=2}^{\infty} Z_n n(n-1)) \\ ((\sum_{n=3}^{\infty} Y_n n(n-1)(n-2)) - K_T) & ((\sum_{n=3}^{\infty} Z_n n(n-1)(n-2)) - K_T) \\ \sum_{n=0}^{\infty} Y_n & -K_T \sum_{n=0}^{\infty} Z_n \end{vmatrix} = 0 \quad (28)$$

Flexible-clump weight (case 5)

$$\begin{vmatrix} \frac{K}{2} & -1 & 0 \\ d & e & f \\ h-a & i-b & j-c \end{vmatrix} = 0 \quad (29)$$

$$a = K_T \sum_{n=0}^{\infty} X_n, \quad b = K_T \sum_{n=0}^{\infty} Y_n, \quad c = K_T \sum_{n=0}^{\infty} Z_n, \\ d = \sum_{n=2}^{\infty} X_n n(n-1),$$

where $e = \sum_{n=2}^{\infty} Y_n n(n-1)$, $f = \sum_{n=2}^{\infty} Z_n n(n-1)$,

$$h = \sum_{n=3}^{\infty} X_n n(n-1)(n-2),$$

$$i = \sum_{n=3}^{\infty} Y_n n(n-1)(n-2), \quad j = \sum_{n=3}^{\infty} Z_n n(n-1)(n-2)$$

Pinned-clump weight (case 6)

$$\begin{vmatrix} (\sum_{n=2}^{\infty} X_n n(n-1)) & (\sum_{n=2}^{\infty} Z_n n(n-1)) \\ ((\sum_{n=3}^{\infty} X_n n(n-1)(n-2)) & ((\sum_{n=3}^{\infty} Z_n n(n-1)(n-2)) - K_T) \\ -K_T \sum_{n=0}^{\infty} X_n & \sum_{n=0}^{\infty} Z_n \end{vmatrix} = 0 \quad (30)$$

3.3. Analytical results

By inputting the material properties and the model scantlings shown in Table 1 with the added mass coefficient and adapted drag coefficient projected from numerical simulation results into the analytical solutions, the natural frequency, in the form of a complex number, can be obtained for each corresponding case. The instability of the riser can be determined by plotting its natural frequency parametrically in an Argand diagram. The correlation between the natural frequency and the eigenvalues of the solutions is conditioned as $\omega = i\lambda$. The instability takes place when the imaginary part of the natural frequency is negative.

This section is to particularly interpret the result of the analytical simulations. The simulation is done for pipes A4-C4 but to emphasize the explanation, the concentration, as a sample, will be focused on the pipe A4. Figs. 3–5 show the Argand diagram for Pipe A4 with fixed at the top-end and clump weight ($K_c = 0.1$) at the bottom for mode 1, mode 2 and mode 3 respectively.

Firstly, by imposing zero fluid velocity and zero adapted drag coefficient, the real value of the natural frequency for all modes of interest can be assessed. The solver uses this value as a first hint to determine the natural frequency for the next conditions. Then by keeping zero fluid velocity but setting the adapted drag coefficient as projected

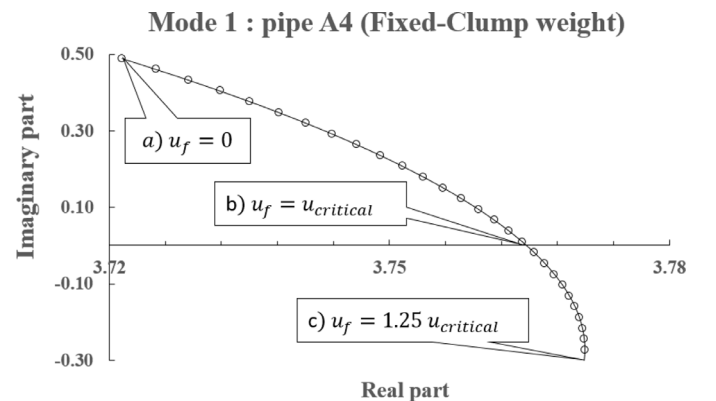


Fig. 3. Argand diagram mode 1 for pipe A4 (Fixed-Clump weight).

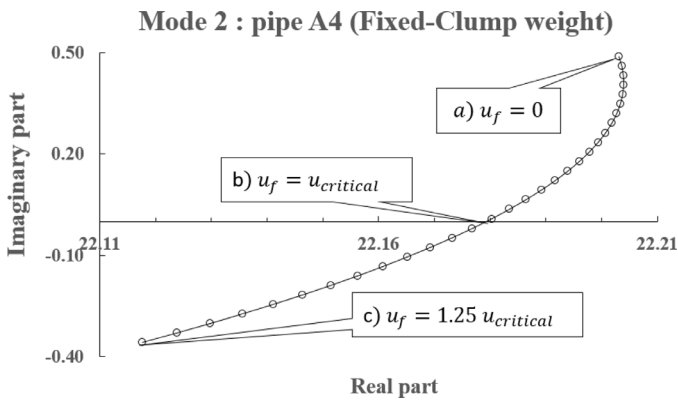


Fig. 4. Argand diagram mode 2 for pipe A4 (Fixed-Clump weight).

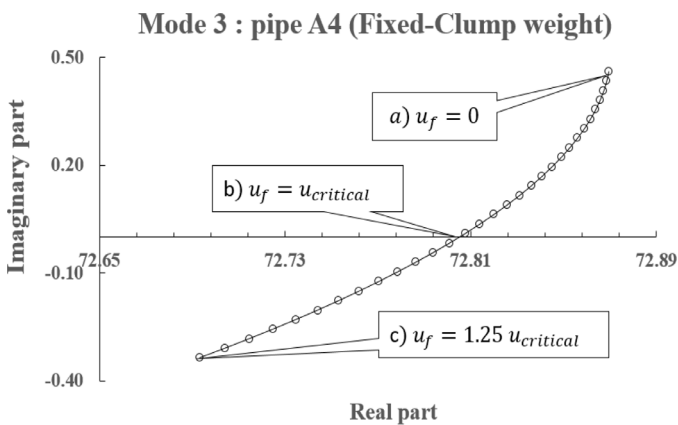


Fig. 5. Argand diagram mode 3 for pipe A4 (Fixed-Clump weight).

from the numerical simulation, point a ($u_f = 0$) in Figs. 3–5 can be assessed. The next step is gradually increasing the seawater velocity resulting decrement of the imaginary part. The critical velocity occurs when the imaginary part of the natural frequency reaches zero point (point b in Figs. 3–5, $u_f = u_{critical}$). The simulation continues until the seawater velocity of 1.25 times of the critical velocity (point c in Figs. 3–5, $u_f = 1.25 u_{critical}$).

Extracting Figs. 3–5, the real and the imaginary frequency versus the dimensionless velocity can be plotted as shown in Figs. 6 and 7. In Fig. 6, at relatively small velocity, the imaginary part of the natural frequency is about the same for all types of boundary conditions, but the gap enlarges remarkably by increasing of the seawater velocity. On the other hand, Fig. 7 shows that the real part of the frequency seems

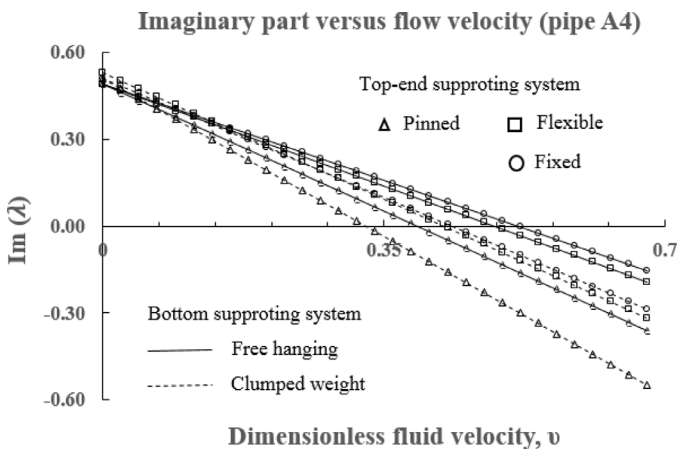


Fig. 6. Imaginary part versus flow at mode 1 for pipe A4.

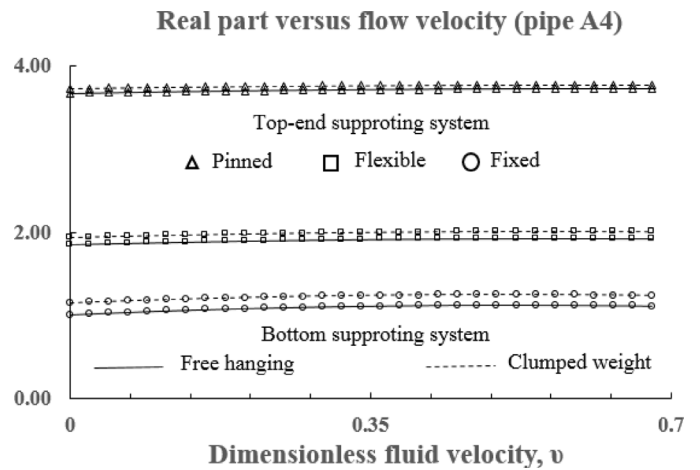


Fig. 7. Imaginary part versus flow at mode 1 for pipe A4.

not affected by the increase of the seawater velocity. The effect of the bottom end supporting system condition is very small compared with the effect of the top-end supporting system.

Setting the weight of the clump as 0%, 10% and 100% of the bare-riser weight, W_r , the effect of the clump weight installation to the mode shapes can be simulated. Fig. 8 shows the first three mode shapes. When the weight of the clump is set as 0%, the model resembles a cantilevered riser. The clump weight tends to drag the bottom-end of the riser to the center of vibration. At a small value, the clump weight will decrease the

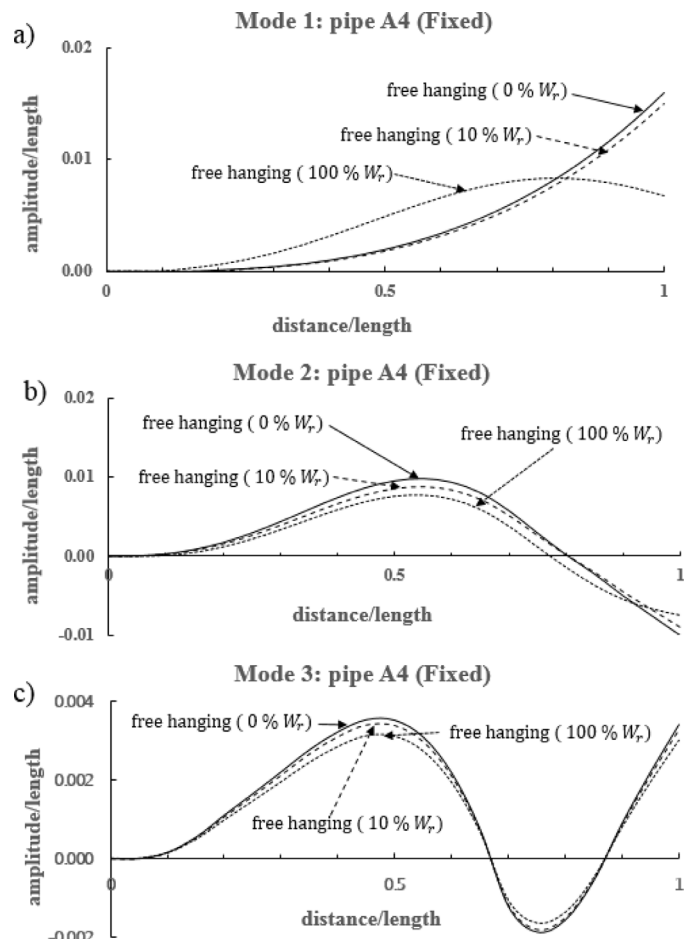


Fig. 8. The shape of modes 1, 2 and 3 for A4 (Fixed- No clump weight; velocity 6 m/s).

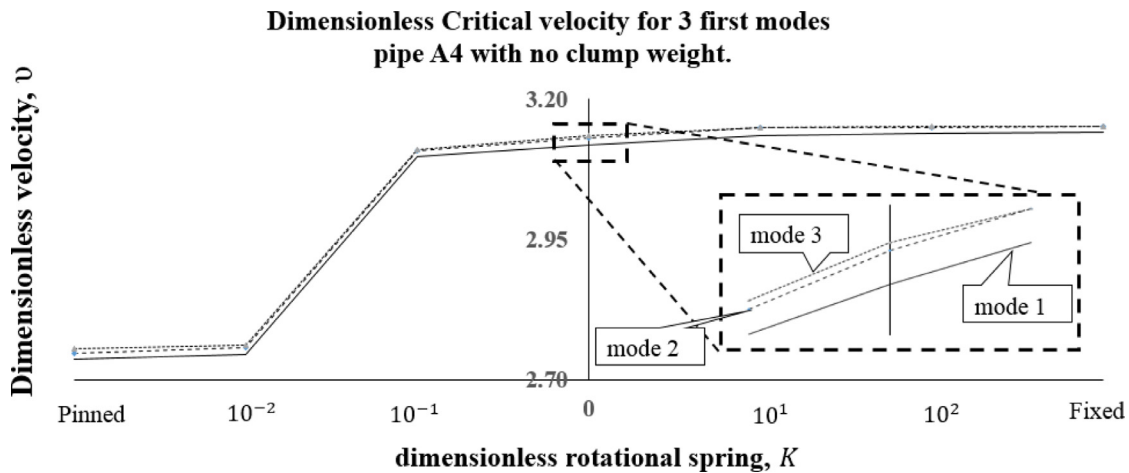


Fig. 9. Critical velocity (m/s) for various conditions of top-end joint observed in pipe A4 with no clump weight.

motion amplitude. At a certain larger value, the clump weight is able to change the mode shape of the vibration, clearly can be seen through Fig. 8a. From Fig. 8, the influence of the clump weight has a greater effect on the lower mode shapes compared with the higher ones. We also can find that large value of the clump weight may make the maximum amplitude in the mode 1 does not always happen at the end-tip of the riser but take places somewhere upper part. Considering this observation results, the critical region set in the numerical simulation will be defined at $0.7 < z/L < 1$.

To investigate the effects of the end-tip boundary conditions to the critical velocity at the first three modes shapes, Figs. 9 and 10 are produced. Fig. 9 is for the top-end joint connection and Fig. 10 is for bottom supporting system condition are produced. In Fig. 9, free hanging (no clump weight) pipe A4 is used and the top end joint is set as fixed, pinned and flexible joint with dimensionless stiffness, K of 0.01, 0.1, 1, 10 and 100. Theoretically, very high-value K , the flexible joint can be seen as a fixed joint. On the contrary, very low of flexible joint assembles the system of the pinned joint.

From Fig. 9, it is shown that the effect of the top-joint connection to the critical velocity is not small, with range about 15% between pinned and fixed joint. The dependence of the critical velocity is very weak for very small and very high K but very sensitive for $10^{-1} \leq K \leq 10^1$. How the critical velocity behaves due to variation of flexible joint stiffness acquired here agrees well with the existing theory on pipe conveying fluid as can be found in [25].

In Fig. 10, pipe A4 with fixed at the top and clump weight installation at the bottom is investigated to observe the effect of the

clump weight to the critical velocity behavior. The dimensionless parameter of the clump weight, K_c is set as 0, 0.026, 0.052, 0.08 and 1.05 which corresponds to the 0%, 25%, 50%, 75%, and 100% of the pipe weight respectively. From the results, it can be concluded that installing clump weight at the bottom of the pipe can effectively increase the stability of the pipe. Considering Figs. 9 and 10 together, they inform that the critical velocity of the mode 1 is smaller compared with the other modes. Since the most crucial critical velocity happens in mode 1, here onwards, the analytical analysis will be used as the basic observation.

4. Numerical simulations

The main aims of the numerical simulations are to obtain the values of the added mass coefficient, adapted drag coefficient, stress at top-end connection, vibration frequency and the vibration amplitude at the bottom end of the pipe through mode shape observation. The values of the added mass coefficient and adapted drag coefficient will be used as input data for the analytical simulation. The values of the maximum stress, vibration frequency, and the vibration amplitude are intended to verify the feasibility of the analytical solution.

4.1. Numerical simulation procedures

The challenges in the numerical simulation for OTEC CWP application is mainly due to the large size of the analyzed models. Even after being scaled down with scale factor 0.1, the length of the pipe is 100 m,

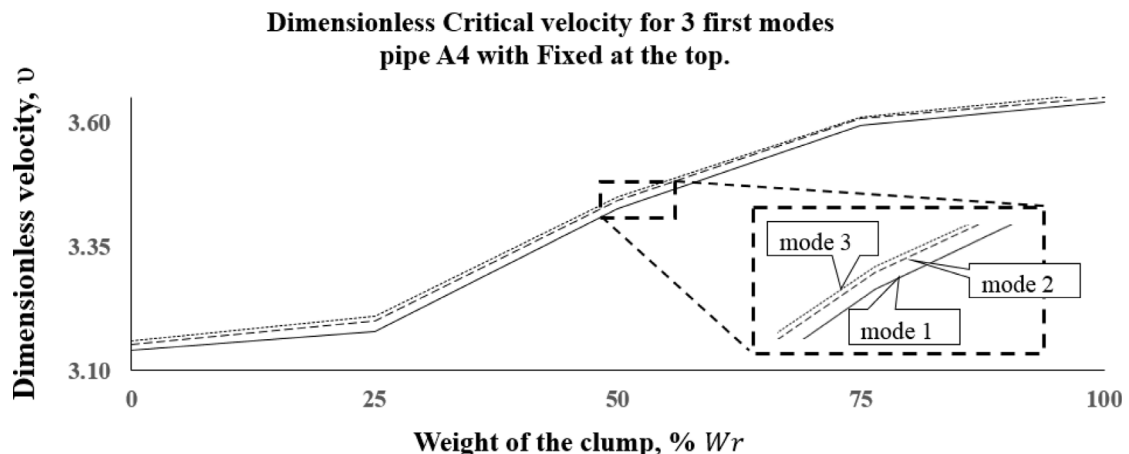


Fig. 10. Critical velocity (m/s) for various values of dimensionless clump weight variable observed in pipe A4 with fixed at the top.

together with the fluid domain, the size of the numerical model will be 125 m length. At this point, the efforts put on this numerical simulation are not merely to obtain the designated results but also how to minimize the computational efforts and the consumed time.

The numerical simulation here is done by combining together the structural analysis software and computational fluid dynamics software or commonly known as fluid-structure interaction (FSI) analysis. In order to ease the pipe model validation, the decoupled analysis is firstly carried out in the Computational Structural Mechanics (CSM). Without considering any applied loads nor any excitations, the mechanical characteristics of the pipe can be computed and the results can be straightforwardly compared with the results from settled theories. After ensuring the acceptance of the pipe model, the FSI analysis procedure can be started. The step by step procedure is extended in the following explanations.

Firstly, as a physical profile, for each model, a pair of pipe and fluid domain is created. Fluid domain is geometry which surrounds the solid pipe including the geometry inside and outside of the pipe. The contact surface between the pipe and the fluid domain is then later set as FSI interface. During the definition process of the pipe, the fluid domain is set to be in a frozen mode. To simplify the simulation procedure, the origin point is located at the center of the outlet area and symmetry condition is imposed along YZ-plane for all analysis step. The detailed geometry and the meshing model are shown in Fig. 11.

The next is the meshing step. This step will significantly influence the simulation results. No matter how advanced the simulation setting, without proper meshing procedure and representative convergence meshing size, satisfying results cannot be obtained. As the geometry of the solid pipe is very simple, its meshing process can be directly produced by using Ansys meshing provided by Ansys interface. But for the fluid domain, the meshing is done using stronger meshing software named ICFM CFD™. To reduce the computational efforts without any disturbance in the simulation process, the critical regions such as the bottom-end of the pipe and fluid domain around the FSI surface are meshed in fine meshing condition and other parts are left in rough meshes. Later in the analysis process, meshing elements of the solid pipe will be considered as finite elements and the meshing elements of the fluid domain will be treated as finite volumes. In order to conduct the fully-coupled FSI simulation, the mesh setting for both solid pipe and fluid domain must be set to allow mesh deformation.

Separately from the fully-coupled analysis, the next particular step is intended to validate the solid model via ANSYS structural simulation specifically using Modal analysis. From this analysis, the modal frequencies and mode shapes of the system can be assessed. After being compared with the settled related theories, the model will then be used for fully-coupled analysis using Transient Structural. The Transient Structural analysis allows the system to be investigated in a function of time. This analysis is relatively complex with many requirements to be undertaken including the time-step input, the physical damping and convergence criteria. The detailed explanation about this procedure can

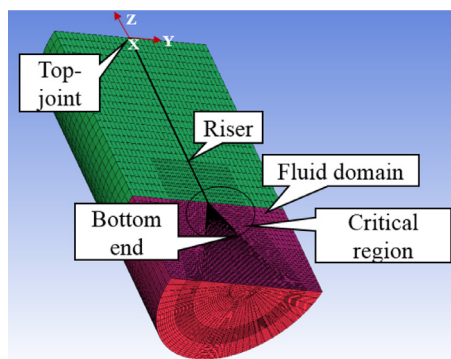


Fig. 11. Geometry and mesh modeling.

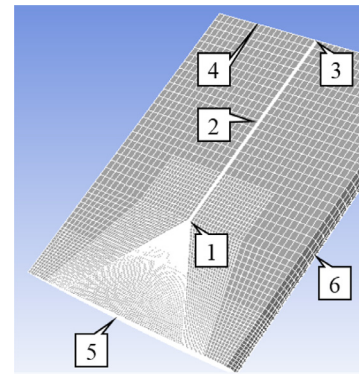


Fig. 12. Boundary conditions numbering.

be found in [14].

Stepping up from the mechanical analysis, the next step is set-up for fluid dynamic analysis using CFX-Pre which is also available in ANSYS Interface. All works correlated with fluid properties are done here. In this step, the boundary conditions of all surface on the fluid domain are defined. The details are numbered in Fig. 12 and listed in Table 2.

At the top surface of the solid pipe, the boundary condition is imposed in either fixed, flexible or pinned joint. On the other parts of the pipe (bottom cross-section surface, inner and outer walls), the surfaces are defined as FSI interface between the solid pipe and the fluid domain. It is also important to be noted that for cases where the pipe is equipped with a clump weight at the bottom end, the clump structure is treated as part of the pipe. Thus, in this case, at the bottom part of the pipe where the clump weight exists, the outer wall refers to the outer surface of the clump weight instead of the outer pipe wall.

For the boundary conditions of the fluid domain, there are several important definitions to set the simulation. All surfaces of the model must be defined based on the desired condition. The top-end of the fluid inside the pipe is defined as an 'Outlet'. 'Outlet' is a boundary condition which allows the fluid to flow out of the surface. The opposite is the 'Inlet' which is set at the bottom end of the fluid inside the pipe. To model the keel of the floating structure, the top-end of the fluid outside the pipe (tank cover) is defined as a 'Wall'. A 'Wall' is intended to duplicate the condition where the surface behaves rigid, no deformation takes places. Finally, the surrounding tank walls are set as an 'Opening' to imitate the open water condition of the sea. 'Opening' is a type of boundary condition to allow the fluid to pass in or pass out to the system depending on the pressure inside and outside of the wall. To model the internal flow, the $k - \epsilon$ model is imposed as the turbulence modeling which is recommended to obtain high accuracy simulation [26].

4.2. Numerical simulation results

Numerical simulation is done for pipes A1-3, B1-3, and C1-3 in various boundary conditions as mentioned in Section 2. In this particular section, the discussion will be focused only for pipes A and C. Pipe A represents high-density material and pipe C is the representative of low-density material.

To calculate the added mass coefficient, a simplified formula proposed by Cimbalá is used [27,28]. This method assesses the added mass by considering the kinetic energy change of the ambient fluid due to change of the pipe's vibration velocity. Mathematically, the equation can be written down as

$$m_{added} = \frac{2(EK_2 - EK_1)}{V_2^2 - V_1^2} \tag{31}$$

EK_1 is the kinetic energy of the surrounding fluid at pipe's movement speed V_1 . While the velocity of seawater transport increases, the pipe

Table 2
Boundary conditions of the simulation model.

Location	Structure Boundary condition	Motion	Fluid Boundary condition	Motion
Bottom-end (1)	FSI interface	Fluid-dependent	Inlet	Received from structure
Inner/outer pipe (2)	FSI interface	Fluid-dependent	FSI interface	Received from structure
Top-end (3)	Fixed, Pinned, Flexible	Based on cases	Outlet	Based on cases
Tank cover (4)			Rigid wall	Fixed
Tank surroundings (5 and 6)			Opening	Flow passes in

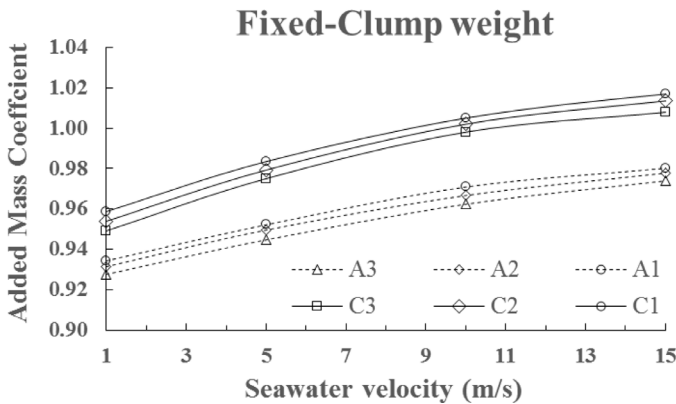


Fig. 13. Effect of material and seawater velocity to the added mass coefficient.

vibrates at a velocity V_2 and the kinetic energy become EK_2 . Using Eq. (31), the added mass can be obtained and then divided with the displaced fluid mass to calculate the added mass coefficient.

To figure out which parameters affect the added mass coefficient at most, Figs. 13–15 are plotted as sample results for particular cases. Fig. 13 shows the effect of the material properties on the added mass coefficient in an incremental increase of seawater transport velocity. In Fig. 13, the boundary condition is set as fixed at the top with clumped weight at the bottom-end. Fig. 14 shows how the added mass behaves due to clump weight installation observed using pipe C and fixed joint at the top-end. Fig. 15 shows the effect of scale factor and top joint conditions to the added mass coefficient under clump weight installation on pipe A. From Figs. 13 and 14, it can be predicted that the added mass is mostly influenced by the material properties, clump weight installation and seawater transport velocities. In the case of scale factor and top joint connection, as shown in Fig. 15, their effect is relatively small.

To get a more accurate conclusion, the obtained data of the added mass coefficient with all of the parameters are observed using statistical analysis. Identical with the results from visual observation, the results from the statistical analysis state that the seawater transport velocities,

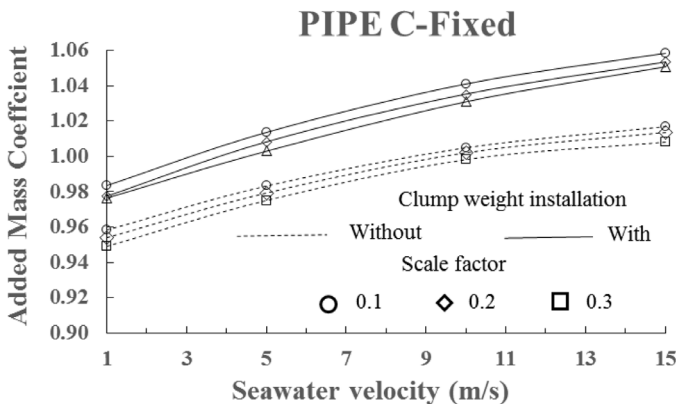


Fig. 14. Effect of clump weight installation to the added mass coefficient.

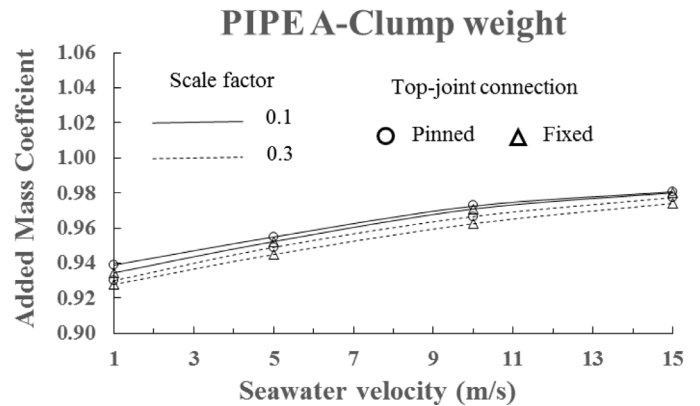


Fig. 15. Effect of scale factor and top-joint connection to the added mass coefficient.

material properties, and clump weight installation affect the added mass coefficient with the percentage of 43%, 26%, and 22% respectively. The rest 9% is the sum up contribution of the scale factor and top joint connection.

The investigation on the added mass coefficient is continued by considering the relation between the dynamic behavior of the pipe and the added mass coefficient. As shown in Fig. 16, considering the coefficient of determination of R^2 , the primary parameter which influences the added mass coefficient is the dimensionless amplitude of the pipe vibration, which of course, the vibration amplitude also depends on the parameters such as material properties, etc. Simply stating, the material properties, clump weight installation, and seawater transport velocity influence the dimensionless vibration amplitude and then, after all, the vibration amplitude affects the added mass coefficient. This point agrees with the previous study on added mass behavior of oscillating body mentioning that the motion amplitude can affect the added mass coefficient [29,30].

The second product is the adapted drag coefficient. As in the analytical model, the solution is derived using the linearized solution, the

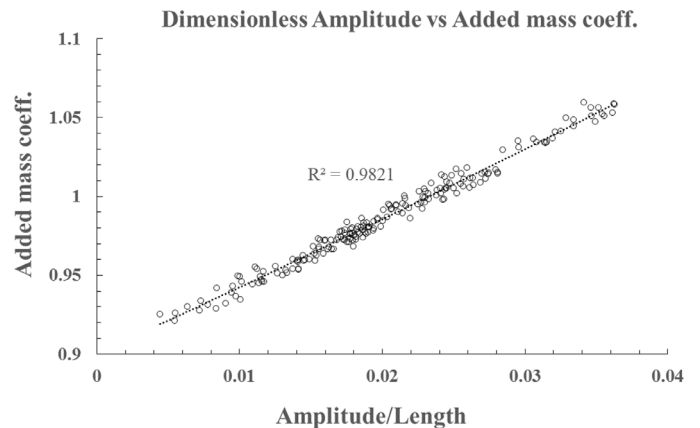


Fig. 16. Effect of motion amplitude to the added mass coefficient.

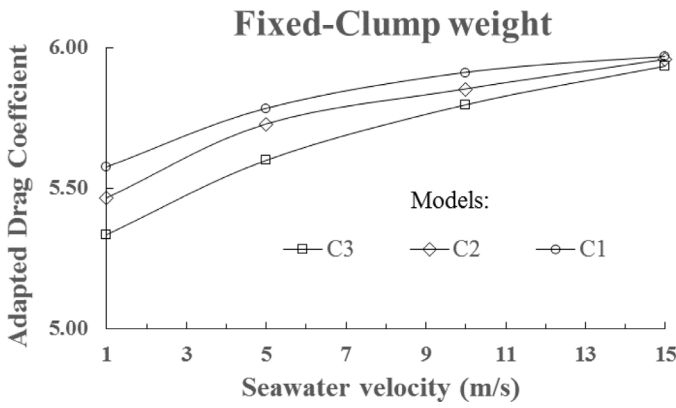


Fig. 17. Effect of material and seawater velocity to the adapted drag coefficient.

desired component of the drag force is the adapted drag coefficient $C_d|V|$ instead of the dimensionless drag coefficient C_d . The equation to calculate the adapted drag coefficient is as follows [31]

$$C_d|V| = \frac{2F_d}{\rho_f AV} \quad (32)$$

F_d is the force component obtained from numerical simulation, ρ_f is the ambient fluid density, A is the reference area and V is the motion speed of the pipe at the bottom-end relative to the fluid velocity surrounding the pipe.

In the aim to investigate the contribution of the case variables to the adapted drag coefficient, the procedures used to produce Figs. 13–15 are repeated which resulting Figs. 17–19. From the visual observation on Figs. 17–19 and statistical analysis, the results are similar to the case of the added mass coefficient. The adapted drag coefficient is mainly affected by the material properties, clump weight installation and seawater velocities. The effects of scale factor and top joint connection are relatively unremarkable. Comparing between Figs. 17 and 18 with Fig. 19, the adapted drag coefficient of pipe C is about ten times higher compared with pipe A. This is because pipe C has a very light density which makes its vibration velocity higher compared with vibration velocity of pipe A.

To get the primary parameter which influences the adapted drag coefficient is little complicated as its value also depends on the motion velocity of the pipe. Using the statistical programming aided analysis, the adapted drag coefficient is transformed into dimensionless adapted drag coefficient as

$$\xi^* = \rho_f D_o \tilde{C}_d L^2 / \sqrt{EI m_r} \quad (33)$$

ξ^* is the dimensionless adapted drag coefficient (the dimensionless adapted drag coefficient here differs with the adapted drag coefficient

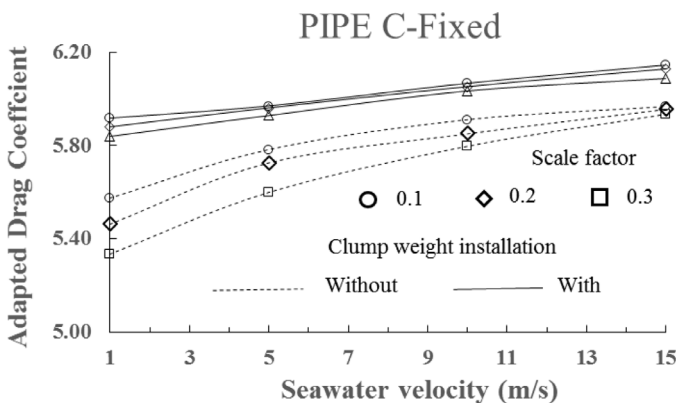


Fig. 18. Effect of clump weight installation to the adapted drag coefficient.

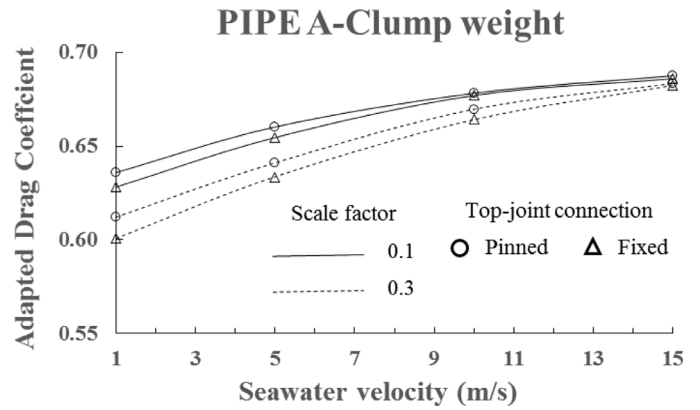


Fig. 19. Effect of scale factor and top-joint connection to the adapted drag coefficient.

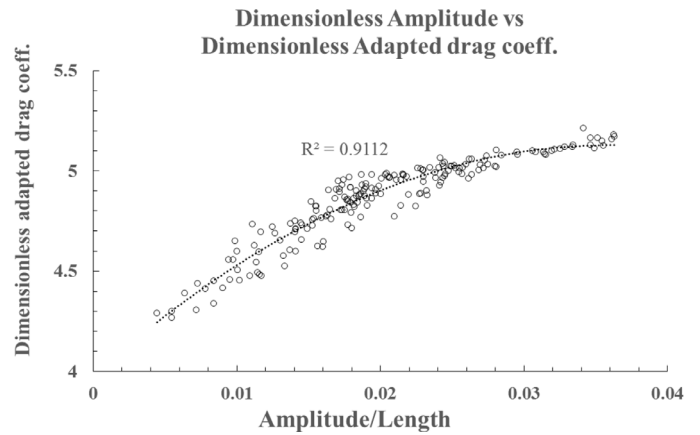


Fig. 20. Dimensionless amplitude versus dimensionless adapted drag coefficient.

in the analytical solution), D_o is the outer diameter of the pipe, \tilde{C}_d is the adapted drag coefficient, L is the riser length, EI is the flexural rigidity and m_r is the riser mass per unit length. The result is shown in Fig. 20.

Based on Fig. 20, referring Eq. (33), it can be understood that the correlation between the dimensionless motion amplitude and adapted drag coefficient highly depends on the material properties and the geometry.

Fig. 21 shows the correlation between seawater transport velocity and dimensionless motion amplitude which is defined as the ratio between vibration amplitude at the bottom-end over the pipe length. To observe the critical velocity point through the incremental increase of

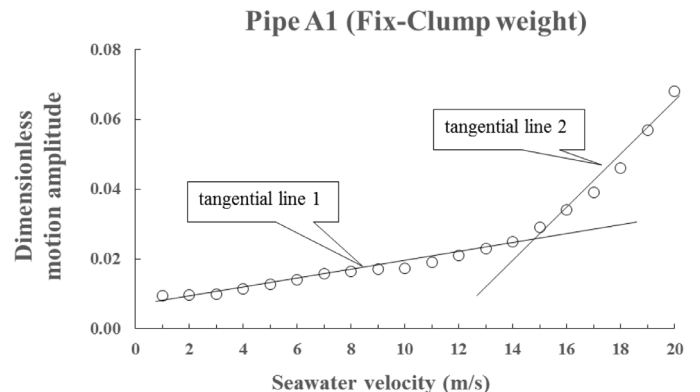


Fig. 21. Dimensionless amplitude versus seawater velocity for pipe A1 (Fixed-Clump weight).

motion amplitude due to an increase of seawater transport velocity is merely hard. For convenience, a conventional bifurcation curve is derived to observe the sudden point where the motion amplitude behaves sensitively toward seawater velocity. Instead of a single point, for more cautiously covering the possible critical velocity, the critical points will be set in range. From Fig. 21, as predicted, the instability does occur at a certain velocity. At low seawater velocities, the increment of motion amplitude is relatively small, skeptically affected to the change of seawater velocity. After hitting its critical velocity, the motion amplitude becomes susceptible and exponentially aggravated. By bifurcation curves, the critical velocity can be easily determined between 14 m/s and 15 m/s. The similar procedures are repeated to determine the critical velocity for other case configurations.

5. Analytical and numerical results comparison

The subject of this section is to judge the acceptance of the analytical model before being used to analyze the pipe in full-scale size. The comparison includes the mode shape, top joint stress, and the critical velocity for pipes A4, B4, and C4 in various end tip boundary conditions. For the numerical analysis, the mode shape and top joint stress can be directly obtained from the simulation. The critical velocity can be also observed using bifurcation curves as explained in Section 3.2. But for the analytical simulation, as the final results strongly depend on the input data, more efforts are necessary to ensure that the input data are correct and meticulous especially for the value of the added mass coefficient and the adapted drag coefficient.

The value of the added mass coefficient and adapted drag coefficient of pipes A1-3, B1-3, and C1-3 are plotted versus each variable e.g. added mass vs scale factor, added mass vs seawater velocity, adapted drag coefficient vs scale factor, etc. From the graph, an equation correlating the added mass coefficient or the adapted drag coefficient with the observed variable can be derived. The equation is then used to project the added mass and adapted drag coefficient of pipe A4, B4, and C4. Then, the projected added mass coefficient and adapted drag coefficient are compared with the numerical results of the same pipes. The results show that the difference between the projected ones and the measured using numerical simulation is averagely only 2%, which is definitely a good agreement. Furthermore, the result also emphasizes the conclusion derived from the numerical simulation results in Section 3.2 that the value of the added mass coefficient and the adapted drag coefficient are influenced by the material properties, clump weight installation and seawater velocities but unremarkable by the top-joint connection and scale factor.

Inserting the projected added mass coefficient, adapted drag coefficient, material properties and the scantlings for particular cases, the mode shapes and the critical velocity can be obtained via analytical simulation. Figs. 22 and 23 show the mode shape comparison of pipe

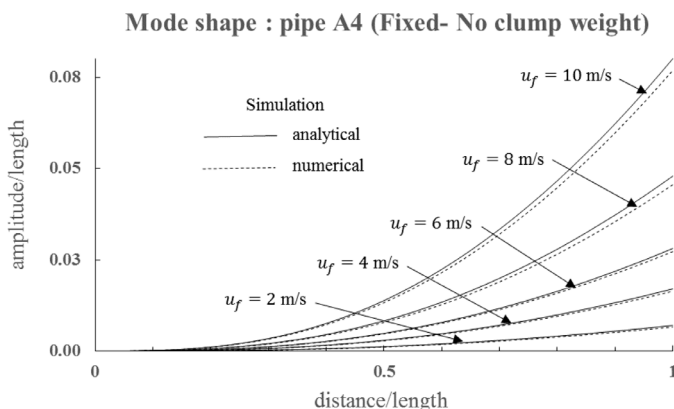


Fig. 22. Mode shape for pipe A4 (Fixed- No clump weight).

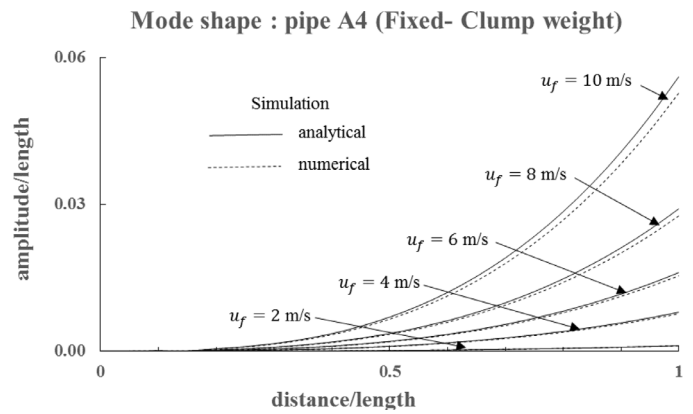


Fig. 23. Mode shape for pipe A4 (Fixed- Clump weight).

A4 (fixed top-bottom free) and pipe A4 (fixed top-clump weight, $K_c = 0.052$) respectively. Numerical simulation results show that without any advanced treatment, the vibration of the pipe naturally behaves in mode 1.

Taken the data together, the mode shapes obtained from the numerical simulation and analytical simulation agree with each other well with the gap of 3%–6% in which the analytical results over-estimates the numerical ones. The effects of the clump weight to the motion amplitude can be found very significant. It can decrease the motion amplitude of up to 30%. Of course, it also depends on the size of the clump weight and the other variables. With clump weight installation (see Fig. 23), the motion amplitude is close to zero for very small seawater velocity.

From Figs. 9 and 10, the critical velocity for Fig. 22 is 7.17 m/s and for Fig. 23 is 8.04 m/s. Before reaching its critical point, the increase of the motion amplitude is very small. But after hitting the critical state, sharp amplitude rise takes place.

Except for the axial loads due to self-weight, the riser is also subject to bending stress due to beam motion. The axial loads are distributed uniformly on the entire cross section. In case of the bending stress, the maximum stress, either in tension or compression, will be on the outer surface of the pipe. As both stresses act normal to the cross-section, the resulting stress will be the combination of the two separate stresses $\sigma_A + \sigma_B$. The equation to calculate the axial stress σ_A is calculated as

$$\sigma_A = T_Z / A_r \tag{34}$$

where T_Z is the tension at point z including the clump weight which is calculated as $(\rho_r - \rho_f)A_r g(L - z) + W_c$, and A_r is the cross-sectional area of the pipe. The bending stress σ_B is calculated as

$$\sigma_B(z) = E \frac{\partial^2 w(z)}{\partial z^2} \frac{D_o}{2} \tag{35}$$

E is the modulus elasticity of the material. Simply speaking, the bending stress depends on the second derivative of the motion displacement as a function of z . In the top fixed configuration, the bending stress maximum occurs at the top end joint which literally the maximum stress will also occur at the top end joint. But for other types, the maximum bending moment is located somewhere along the pipe. In this case, the maximum stress is observed at a point in which $-(\rho_r - \rho_f)A_r g + \partial^3 w(z) / \partial z^3 = 0$.

The final comparison results are shown in Tables 3 and 4 for the critical velocity and top stress respectively. In Table 3, for the boundary condition, stiffness of the flexible joint at the top is set as $K = 1$ and the clump weight is 50% of riser weight for heavy material (Steel and aluminum) and 100% of riser weight for FRP. The results show that the critical velocity predicted by analytical simulation is all in range of the critical velocity predicted by numerical simulation. The difference is only 2–6% if the analytical results are compared with the mid-value of the numerical ones. For the material choice comparison, the table

Table 3
Critical velocity (m/s) comparison for pipe with scale factor 0.4.

End tip boundary condition	Pipe A4		Pipe B4		Pipe C4	
	Ana.	Num.	Ana.	Num.	Ana.	Num.
Pinned-free	7.99	7.4–8.2	6.02	5.5–6.6	4.21	3.7–4.4
Flexible-free	9.04	8.1–9	7.81	7–8.8	5.8	5.4–6.6
Fixed-free	9.17	8.5–9.5	8.76	8.1–9	6.31	6.1–7.1
Pinned–Clump weight	10.04	9.4–10.4	9.91	9.5–10.4	7.41	7.8–7.5
Flexible–Clump weight	11.01	10.3–11.4	10.88	10.3–11.4	9.23	9–10.6
Fixed–Clump weight	12.6	12–13	11.23	10.7–11.4	10.2	9.6–10.4

Table 4
Top stress over yield stress and motion frequency comparison for pipe in top-fixed configuration with scale factor 0.4 observed at critical velocity.

Pipe	Method	T_{top}/σ_{yield}		Frequency of the first mode (Hz)	
		Fixed-free	Fixed-clump	Fixed-free	Fixed-clump
A4	Ana.	0.361	0.321	0.72	0.54
	Num.	0.366	0.328	0.77	0.56
B4	Ana.	0.142	0.098	0.84	0.61
	Num.	0.148	0.102	0.86	0.65
C4	Ana.	0.084	0.073	1.36	0.98
	Num.	0.087	0.075	1.42	1.02

indicates that the critical velocity of steel material is above compared with others. In instance, it can be said that the critical velocity increase by increasing the value of $m_r/(m_f + m_r + m_a)$ and the value of flexural rigidity, for which already well-known from the general knowledge on pipe aspirating behavior [25].

Table 4 shows the comparison results for the top joint stress and motion frequency. The comparison is only done for the top-fixed joint and the weight of the clump is 50% of riser weight. In general, the top stress predicted by the analytical simulation is 3%–6% lower compared with the ones obtained from the numerical simulations. Regarding the effect of the clump weight installation, it is able to decrease the top stress, of course, the stress due to axial strain gets higher but the bending stress lessens more than the increase of the axial stress. The decrease of the bending stress is due to the capability of the clump weight to decrease the motion amplitude. In the case of the frequency comparison, from Table 4, the results obtained from the analytical and numerical simulation are very close. The table also shows that the clump weight can also decrease the motion frequency.

Taken Tables 3 and 4 together, in the view of critical velocity, the heavy materials are better as they are more stable and the motion amplitude is less. But considering the top stress, heavy material makes the top-joint suffer from the large stress. From the tables, the suggestion is to use light materials (FRP) with clump weight installation. The light material choice is intended to minimize the top stress and the clump weight installation is to stabilize the system. More strictly consideration, in the top-fixed configuration, for the FRP, by installing clump weight, the critical velocity increases up to 50% and the top stress decreases up to 30%. The sensitivity of the critical velocity and the top joint stress on the clump weight installation effect definitely also varies

Table 5
Analytical results of full-scale models.

Material	End-tip configurations		Critical velocity (m/s)	$\frac{T_{top}}{\sigma_{yield}}$	Note	Frequency of the first mode (Hz)
	Top-joint	Clump weight (% W_r)				
Steel	Pinned	50	1.4	0.7	Not accepted	0.86
Aluminum	Pinned	50	2.2	0.66	Accepted	0.975
FRP	Flexible $K = 0.1$	50	2.3	0.237	Accepted	1.725
	Flexible $K = 0.1$	100	2.8	0.217	Accepted	1.561
	Flexible $K = 1$	100	3.95	0.261	Accepted	1.224
	Pinned	100	3.2	0.156	Accepted	1.975
	Pinned	150	3.6	0.128	Accepted	1.806

depending on the other type of boundary condition. But generally speaking, it can be used as a clue that clump weight installation give significant effects to the critical velocity.

As final conclusion of the comparison study, considering the gap between analytical results and numerical results, it can be concluded that the analytical solution is accepted enough to be used for the full-scale models.

6. Full-scale models analysis

The next step of the analysis is carrying out the analytical simulation for the full-scale model. The scantling and material properties are shown in Table 1. For all pipes models, in case of the flexible joint at the top, the stiffness K , is varied from 0.01 to 100 with an increment of the logarithmic scale base 10. For the clump weigh, its weight over the riser weight is set as 25% to 150% with an increment of 25%. The step by step procedure to undergo the analytical solution for the full-scale model is exactly the same with the analytical simulation for the scaled model as already explained in Section 3.3.

Considering the critical velocity and the maximum stress, deciding the best solutions through graphical comparison is possible, yet time-consuming and inefficient. To ease, a post-processing program is generated to automatically produce the best solutions. The acceptance criteria include the critical velocity and the top joint stress. The minimum critical velocity is 2.5 m/s, which is 0.5 m/s higher than the required one [3]. The upper limit ratio between the maximum stress over the yield stress is set to be 0.7, which means safety margin of 0.3 is imposed. This number is considered based on the unacceptable consequence of failure and the requirement of underwater accessibility for inspections [32]. In the early stage of the analysis, the analysis finds a condition where the ratio between the maximum stress over the yield stress has reached 0.7 before the velocity has not been beyond its critical value. At this condition, the velocity where the ratio between the maximum stress over the yield stress hits 0.7 is determined as the critical velocity.

Table 5 shows the results of the analytical simulations for the full-scale model. Steel material is not recommended in all case of end-tip boundary conditions. The achieved maximum critical velocity is only 1.4 m/s, which is below the required one. For aluminum, the results state that this material is acceptable for some extents.

The top joint connection must be set in pinned configuration and clump weight must be installed at 50% of bare-riser (without clump weight) weight. Yet, after all, the obtained value is in the precarious stage. The maximum stress is very close to the margin. The most prospective material is FRP, its low material density makes the maximum stress relatively small and its high yield stress make it possible to choose various type of top joint connection. For FRP, the required weight of the bottom clump is at least 50% of the riser weight, which is practically accepted. For the vibration frequency, its value is relatively large, which indicates that the system vibrates fast.

7. Conclusions

The stability analysis of submerged, top-tensioned free hanging riser has been investigated by numerical and analytical methods. The analytical approach is developed by adapting the existing formulation with some modifications by introducing the prospective boundary conditions as efforts to increase the critical velocity and to reduce the top joint stress. The numerical simulation is done using a commercial software Ansys interface. Using scale models, the results obtained from the analytical approach are compared with the results from the numerical ones. The analysis on the analytical and numerical results and the comparison processes are done by utilizing a data processing software Python. Finally, the critical velocity and maximum stress of full-scale models are discussed to determine the most prospective material for OTEC utilization.

From the results obtained by both analytical and numerical simulations, the tendency of the critical velocity behavior on the change of the variables are also compared with the existing theory on riser conveying fluid. It is found that the results obtained here agree well with the existing theory. Comparison study between analytical and numerical simulations states that the analytical results are in good agreement with the numerical ones. The final result is the determination of the most prospective material for OTEC riser. Due to its low density but high yield stress, FRP material will be the most suitable material for OTEC utilization among the other examined materials in this study. Considering the obtained value of the vibration frequency, the fatigue

Supplementary materials

Supplementary material associated with this article can be found, in the online version, at doi:[10.1016/j.apor.2019.101921](https://doi.org/10.1016/j.apor.2019.101921).

APPENDIX A: Analytical and numerical simulation vs. published experimental results

There are several experiment projects on riser conveying fluid having been carried out [15,33,34]. To support the confidence of the developed analytical model, the experimental results from the previous publications will be compared with the results of the analytical or numerical simulation using the proposed model. The configurations of the experimental environment are listed in Table A.1

Based on its flow direction, the models listed in Table A.1 can be divided as pipe aspirating fluid (model 1 and 4) and pipe discharging fluid (model 2 and 3). The developed analytical model in this paper is governed for fluid-aspirating pipe, thus models 2 and 3 (fluid-discharging pipes) will be only used to validate the numerical models. In regards to OTEC application, model 4 has a similar characteristic with the CWP. The comparison results are tabulated in Table A.2.

From the Table A.2, the critical velocity obtained from the analytical and numerical simulation shows a good agreement with the experimental one except model 1. This is because the transported fluid and the ambient fluid in model 1 are the air but the designated internal fluid and external fluid in this study are water. The different characteristic of the models between both fluids might be the reason for these large gaps. However, excluding the model 1 and focusing on model 4, the feasibility of the developed analytical and numerical simulation is proven.

Table A.1

Experimental model configurations from previous publications.

Variables	Model 1 [15]	Model 2 [33]	Model 3 [33]	Model 4 [34]
Pipe				
Length (m)	0.401	0.6096	1.524	0.445
Inner diameter (m)	0.00934	0.0111	0.00791	0.00934
Outer diameter (m)	0.0159	0.0127	0.0095	0.0159
Mass (Kg/m)	0.144	0.0288	0.0256	0.144
Flexural rigidity (Nm ²)	7.63×10^{-3}	4×10^{-1}	1.96	7.28×10^{-3}
Fluid				
Flow direction	Downward	Upward	Upward	Downward
Internal fluid	air	water	water	water
Ambient fluid	air	air	air	water
Supporting system				
Bottom-end	Free	Free	Clumped (W _C =4 N)	Free
Top-end	Fixed	Fixed	Fixed	Fixed

analysis is very crucial to be examined and will be done in the near future.

8. Future work

In this paper, the pipe is simplified as a homogeneous structure. For the future work, the stiffening system will be introduced to support the integrity of the riser from local pressure and local bending moment, especially for a pinned joint where its maximum bending moment takes place not at the top joint but somewhere along the pipe. Additionally, future research will also focus on other excitations such as currents, floating structure motions, vortex-induced vibration, etc. To increase the confidence of the analytical model, the experiment will be conducted in the near future.

After the complete design of the CWP has been proposed and its cost estimation has been assessed, the next works will be around the manufacturing and installation process along with the management and operational analysis including: (1) Axial oscillation due to weather/environmental conditions; (2) Lateral oscillation due to ocean loop current; (3) Failure due to riser emergency disconnect from the top joint connection.

Acknowledgment

This work was supported by Indonesia Endowment Fund for Education(LPDP) [grant number S-619/LPDP.3/2017]

Table A.2
Critical velocity comparison (m/s).

Model	Exp.	Ana.	Num.
1	60	54	52.4
2	31.4	–	29.6
3	18.8	–	17.7
4	3.39	3.28	3.19

References

- [1] L.A. Vega, Ocean thermal energy conversion, in: R.A. Meyers (Ed.), *Encyclopedia of Sustainability Science and Technology*, 6 Springer, New York, 2012, pp. 7296–7328.
- [2] M.L. Syamsuddin, A. Attamimi, A.P. Nugraha, S. Gibran, A.Q. Afifah, N. Oriana, OTEC potential in the Indonesian seas, *Energy Procedia* 65 (2015) 215–222, <https://doi.org/10.1016/j.egypro.2015.01.028>.
- [3] R. Adiputra, T. Utsunomiya, J. Koto, T. Yasunaga, Y. Ikegami, Preliminary design of a 100 MW-net ocean thermal energy conversion (OTEC) power plant study case: Mentawai island, Indonesia, *J. Mar. Sci. Technol.* (2019), <https://doi.org/10.1007/s00773-019-00630-7>.
- [4] G.C. Nihous, L.A. Vega, Design of a 100 MW OTEC-hydrogen plantship, *Mar. Struct.* 6 (1993) 207–221, [https://doi.org/10.1016/0951-8339\(93\)90020-4](https://doi.org/10.1016/0951-8339(93)90020-4).
- [5] A. Miller, M. Ascari, OTEC advanced composite cold water pipe: final technical report, (2011). <https://www.osti.gov/biblio/1024183> (Accessed: 10 March 2019).
- [6] A. Miller, T. Rosario, M. Ascari, Selection and validation of a minimum-cost cold water pipe material, configuration, and fabrication method for ocean thermal energy conversion (OTEC) systems, SAMPE, Proceedings of SAMPE 2012, the Society for the Advancement of Material and Process Engineering, Maryland, 2012, pp. 1–28.
- [7] G.C. Nihous, A preliminary assessment of ocean thermal energy conversion resources, *J. Energy Resour.* 129 (2007) 10–17, <https://doi.org/10.1115/1.2424965>.
- [8] L. Martel, P. Smith, S. Rizea, et al., Ocean thermal energy conversion life cycle cost assessment: final technical report, (2012). <https://www.osti.gov/servlets/purl/1045340> (Accessed: 10 March 2019).
- [9] S. Xiang, P. Cao, R. Erwin, S. Kibbee S, OTEC cold water pipe global dynamic design for ship-shaped vessels, *Ocean Renewable Energy* (volume 8), Proceeding of the 32nd ASME International Conference on Offshore Mechanics and Arctic Engineering, France, 2013 V008T09A060.
- [10] X. He, W. He, Y. Liu, Y. Wang, G. Li, Y. Wang, Robust adaptive control of an offshore ocean thermal energy conversion system, *IEEE Trans. Syst. Man Cybern. Syst.* (2018) 1–11, <https://doi.org/10.1109/TSMC.2018.2870999>.
- [11] W. He, C. Sun, S.S. Ge, Top tension control of a flexible marine riser by using integral-barrier Lyapunov function, *IEEE-Asme T Mech.* 20-2 (2015) 497–505, <https://doi.org/10.1109/TMECH.2014.2331713>.
- [12] M.P. Paidoussis, N.T. Issid, Dynamic stability of pipes conveying fluid, *J. Sound Vib.* 33 (1974) 267–294, [https://doi.org/10.1016/S0022-460X\(74\)80002-7](https://doi.org/10.1016/S0022-460X(74)80002-7).
- [13] D.B. Giacobbi, C. Semler, M.P. Paidoussis, Numerical fluid-structure interaction study of a cantilevered pipe discharging or aspirating fluid via a computational fluid dynamics and finite element analysis model, in: M. Papadrakakis, B.H.V. Topping (Eds.), Proceedings of the Sixth International Conference on Engineering Computational Technology, Greece, Civil Comp Press, 2008paper 48.
- [14] D.B. Giacobbi, The Dynamics of Aspirating Cantilevered Pipes and Pipes Conveying Variable Density Fluid, M. Eng Thesis McGill University, 2010.
- [15] D.B. Giacobbi, S. Rinaldi, C. Semler, M.P. Paidoussis, The dynamics of a cantilevered pipe aspirating fluid studied by experimental, numerical and analytical methods, *J. Fluid Struct.* 30 (2012) 73–96, <https://doi.org/10.1016/j.jfluidstructs.2011.11.011>.
- [16] G.L. Kuiper, A.V. Metrikine, Dynamic stability of a submerged, free-hanging riser conveying fluid, *J. Sound Vib.* 280 (2005) 1051–1065, <https://doi.org/10.1016/j.jsv.2004.09.024>.
- [17] X. Liang, X. Zha, X. Jiang, L. Wang, J. Leng, Z. Cao, Semi-analytical solution for dynamic behavior of a fluid-conveying pipe with different boundary conditions, *Ocean Eng.* 162 (2018) 183–190, <https://doi.org/10.1016/j.oceaneng.2018.05.060>.
- [18] Z. Wei, L. Ye, W. Xiaoni, G. Shihao, Review of the applied mechanical problems in ocean thermal energy conversion, *Renew. Sustainable Energy Rev.* 93 (2018) 231–244, <https://doi.org/10.1016/j.rser.2018.05.048>.
- [19] A. Abbaslou, M.R. Maheri, Prediction of the damping properties of fiber-reinforced polymer composite panels with arbitrary geometries, *Proc. Inst. Mech. Eng. Part C* 232 (2016) 275–283, <https://doi.org/10.1177/0954406216676506>.
- [20] H. Bachmann, et al., *Vibration Problems in Structures: Practical Guidelines*, Birkhauser Verlag, Berlin, 1995.
- [21] L. Cremer, M. Heckl, *Structure-borne Sound*, Springer-Verlag, New York, 1988.
- [22] W. Qi, X. Xu, Analytical method of dynamic properties of FRP based on micro-mechanical level, *Chin. J. Aeronaut.* 28 (2015) 939–945, <https://doi.org/10.1016/j.cjca.2015.03.008>.
- [23] W. He, S. Nie, T. Meng, Y. Liu, Modeling and vibration control for a moving beam with application in a drilling riser, *IEEE Trans. Control Syst. Technol.* 25- 3 (2017) 1036–1043, <https://doi.org/10.1109/TCST.2016.2577001>.
- [24] T. Huang, D.W. Dareing, Natural frequencies of marine drilling risers, *J. Pet. Technol.* 28 (1976) 813–818, <https://doi.org/10.2118/5620-PA>.
- [25] M. Kheiri, M.P. Paidoussis, Dynamics of a pipe conveying fluid flexibly restrained at the ends, *J. Fluid Struct.* 49 (2014) 360–385, <https://doi.org/10.1016/j.jfluidstructs.2013.11.023>.
- [26] ANSYS inc, ANSYS Software Version 17, ANSYS Help, ANSYS inc, USA, 2017.
- [27] J.M. Cimbala, A new method for calculating added mass using CFD, Proceedings of Division of Fluid Dynamics 56th Annual Meeting, ECT 2008, APS, American Physical Society, New Jersey, 2008KK.007.
- [28] A. Kuessesh, Added mass formulation for fluid structure interaction (MSc Thesis), American university of Sharjah, 2016.
- [29] L. Bonfiglio, S. Brizzolara, C. Chryssostomidis, et al., Added mass and damping of oscillating bodies: a fully viscous numerical approach, in: M.K. Jha, M. Lazard, et al. (Eds.), Recent Advances in Fluid mechanics, Heat & Mass Transfer and Biology, Harvard University Press, USA, 2012, pp. 210–215.
- [30] S. Fackrell, Study of the added mass of cylinders and spheres (PhD Thesis), University of Windsor, 2011.
- [31] G. Bruschi, T. Nishioka, K. Tsang, R. Wang, A Comparison of Analytical methods: Drag Coefficient of a Cylinder, University of California (MAE 171A), California, 2003.
- [32] Det Norske Veritas, *Structural Design of Offshore Units*, DNV, Norway, 2012.
- [33] J.A. Jendrzejczyk, S.S. Chen, Experiments on tubes conveying fluid, *Thin Wall Struct.* 3-2 (1985) 109–134, [https://doi.org/10.1016/0263-8231\(85\)90028-X](https://doi.org/10.1016/0263-8231(85)90028-X).
- [34] J. Stephane, Stability of thick and thin flexible pipes subjected to axial flow (M. Eng Thesis), McGill University, 2011.